

Influence of Adjustable CeO₂ Morphology on the Performance of Ambient Hole Transport Layer-Free Carbon-Based Perovskite Solar Cells

Shubhranshu Bhandari,^{*,#} Sreeram Valsalakumar,^{*,#} Mir Sahidul Ali, Tapas K. Mallick, Justin Hinshelwood, and Senthilarasu Sundaram



Cite This: *Energy Fuels* 2025, 39, 9566–9575



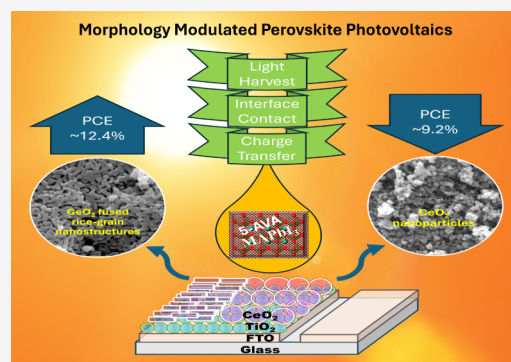
Read Online

ACCESS |

Metrics & More

Article Recommendations

ABSTRACT: The combined effect of TiO₂ and CeO₂ as the electron transport layer (ETL) in the hole transport layer (HTL)-free carbon-based perovskite solar cells (C-PSCs) to enhance performance characteristics is a less explored research area. In this context, we investigated the effect of morphology-tuned CeO₂ in combination with TiO₂ in the C-PSCs. Considering the light scattering effect in C-PSCs and the property of extending the light-traveling distance across the photoelectrode, we synthesized rod and cubic CeO₂ nanostructures. The synthesized nanoparticles were used over the TiO₂ layer, and their photovoltaic performance was compared to that of the TiO₂-only C-PSC and analyzed by using impedance and quantum efficiency studies. The light-scattering effect on the C-PSCs, investigated with the diffused reflectance study, found that the rod structure of CeO₂ provides better light travel toward the photosensitizer, and the highest power conversion efficiency (PCE) of nearly 12.5% was recorded for the rod-shaped CeO₂ in the HTL-free C-PSC, which is 24% higher compared to a pristine TiO₂-based C-PSC. Moreover, the devices with rod-shaped CeO₂ demonstrated suitable charge transport properties along the perovskite layer and a lower charge recombination rate when compared with the cube structure. This work demonstrates a major breakthrough in the performance enhancement of HTL-free C-PSCs by nanomaterial morphology alteration and fabrication engineering, which can significantly influence future research.



1. INTRODUCTION

The rapid development of organic–inorganic carbon-based perovskite solar cell (C-PSC) technology over a decade has gained attention from industrial and academic societies.^{1–4} The noteworthy improvement in power conversion efficiency (PCE) from a single digit to over 26% has been observed for traditional noble metal counter electrode devices, which is the same as the single-crystalline silicon solar cells and 1.7% higher than multicrystalline silicon solar cells.^{5–10} However, HTL-free devices are still hovering around a PCE of 15%.¹¹ The simple solution-based fabrication method and the unique optoelectronic properties of perovskite nanocrystals and allied layers have attracted scientific curiosity among researchers.^{2,8,12–18} The ETL extracts photogenerated electrons from the absorber or the perovskite and transfers them to the TCO layer.^{8,9,15} Considering the importance of ETL material selection in the fabrication process affects the C-PSC efficiency and stability. A wide range of research studies have been conducted with different ETL materials to address interfacial charge recombination between the ETL and the perovskite layer.^{3,5,6,9,15,19–24}

Among the ETL materials, titanium dioxide (TiO₂) is the most used one in the regular architecture of the C-PSCs.^{19,24,25}

Alternatively, other ETL materials, such as ZnO, SnO₂, BaSnO₃, CeO₂, etc., have been utilized in C-PSC fabrication, achieving significant results.^{26–28} The application of different particle sizes and shapes plays a vital role in determining the performance of C-PSCs.^{26,29,30} There have been various studies in terms of the morphology modulation of the ETL and its impact on the PSCs or the C-PSCs.^{19,26,29–34} In 2020, Wu et al. carried out an ETL morphology engineering study to produce TiO₂ nanocrystals, followed by the doping of Zn into the ETL.³⁵ This study demonstrated an average PCE (power conversion efficiency) of 19.87% for Zn-doped nanocrystalline TiO₂ and 16.95% for nondoped normal TiO₂. Also, to evaluate the titania macropores in the TiO₂ layers, in 2021, Khan et al. conducted an extensive study on synthesizing three-dimen-

Received: January 27, 2025

Revised: April 11, 2025

Accepted: April 30, 2025

Published: May 12, 2025



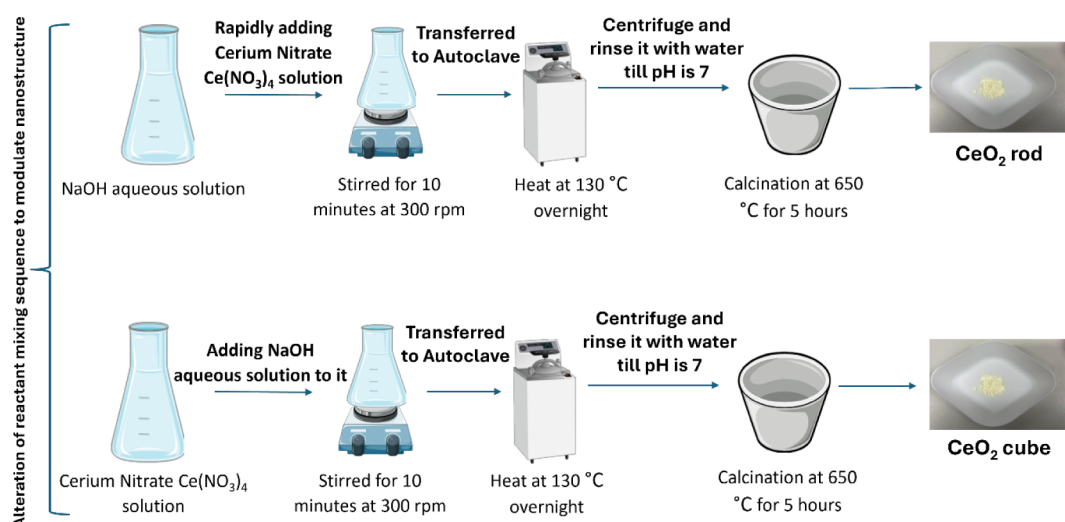


Figure 1. Schematic of CeO₂ nanostructure syntheses for (a) the rod structure and (b) the cube structure by alteration of reactant mixing.

Table 1. Configuration of the Fabricated Perovskite Devices

| Type | C-TiO ₂ | m-TiO ₂ | CeO ₂ Rod | CeO ₂ Cube | Al ₂ O ₃ | Carbon | Perovskite |
|----------|--------------------|--------------------|----------------------|-----------------------|--------------------------------|---------|------------|
| Device 1 | present | present | N/A | N/A | present | present | present |
| Device 2 | present | present | present | N/A | present | present | present |
| Device 3 | present | present | N/A | present | present | present | present |

sional (3-D) hollow anatase TiO₂ microspheres through the hydrothermal method and assessed their suitability as an effective ETL for the C-PSCs.³⁶ In 2020, Wang et al. validated the impact of an amorphous WO_x (a-WO_x) layer as an interlayer between the perovskite and the TiO₂ layers.³⁷ This study clearly indicated better nonwettability performance of the hybrid ETL (TiO₂ + a-WO_x) and the improved crystallization of the perovskite layer via enhancing the grain boundary mobility.³⁷ The C-PSC with the hybrid ETL showed a PCE of 20.98% and 30 days of stability at room temperature under dark conditions.³⁷ In 2022, Bhandari et al. investigated the performance variation of C-PSCs by blending the morphology and the phase of TiO₂.³⁸ This study considered the brookite phase of TiO₂ and recorded the improved efficiency and effects on charge recombination with respect to different morphologies.³⁸ Considering the ETL doping strategies, in 2022, Arshad et al. demonstrated the use of a Ca-doped TiO₂ layer, which was synthesized through the sol-gel method.³⁹ The study indicated the improved performance in the current density, increasing from 15 mA/cm² for the C-PSC with normal TiO₂ to 19.3 mA/cm² for the Ca-doped layer.³⁹ Furthermore, in 2020, Ebrahimi et al. examined the effects of adding the dopant GQDs (graphene quantum dots) in the TiO₂ layer and indicated that pinhole density was reduced on the perovskite film.⁴⁰ This aided the electron extraction and enhanced the charge mobility in the GQD-doped TiO₂ layer.⁴⁰ The EIS (electrochemical impedance spectroscopy) analysis from this study indicated a diminished recombination process in the doped layer compared to the normal layer, which provided an improved FF (fill factor) for the C-PSCs.⁴⁰ Li is a widely used doping agent for TiO₂ layers and several studies have demonstrated performance enhancements due to Li doping.^{29,41–45} In 2020, Teimouri et al. showed increased conductivity and faster electron transport characteristics in the TiO₂ layer through Li doping.⁴⁴ In this study, capacitance-frequency analysis interpreted higher

conductivity and lower trap-state density in the TiO₂/perovskite layers.⁴⁴ However, device engineering using an electron transport material (ETM) can still play a crucial role, as it influences performance in various ways.

In this aspect, we considered the first of its kind, the coupling of morphology-modulated CeO₂ nanostructures with TiO₂ as the combined ETL and conducted performance testing for the ambient HTL-free C-PSC. The C-PSC fabricated with the rod-shaped CeO₂ particles provided better performance than the standard ETL, and the device with cube-shaped CeO₂ particles.

2. EXPERIMENTAL SECTION

2.1. Synthesis of CeO₂ Rods and Cubes. The synthesis method was adapted from previous literature with suitable modifications, as shown in the schematic diagram in Figure 1.⁴⁶ To synthesize the CeO₂ rod particles, cerium nitrate (Ce(NO₃)₃)₄ purchased from Merck was dissolved in deionized (DI) water and rapidly added to 10% NaOH solution and stirred for 10 min at 300 rpm. Afterward, the solution was transferred into an autoclave (130 °C for 24 h), followed by centrifugation and rinsing with water until the pH of the solution reached 7. Finally, the end product from the autoclave was calcined for 5 h at 650 °C.

The alteration of the mixing sequence was followed to synthesize the CeO₂ cube particles. A 10% NaOH aqueous solution was prepared first. In a separate container, cerium nitrate (Ce(NO₃)₃)₄ was dissolved in DI water, and the initially prepared aqueous NaOH was added to it vigorously with continuous stirring for 10 min at 300 rpm. Then, the solution was transferred to an autoclave (130 °C for 24 h), followed by centrifugation and rinsing with water until the pH reached 7. In the end, similar to the CeO₂ rod synthesis, the material underwent the calcination process at 650 °C for 5 h.

2.2. Device Fabrication. The device fabrication methodology was adopted from previously published articles, and

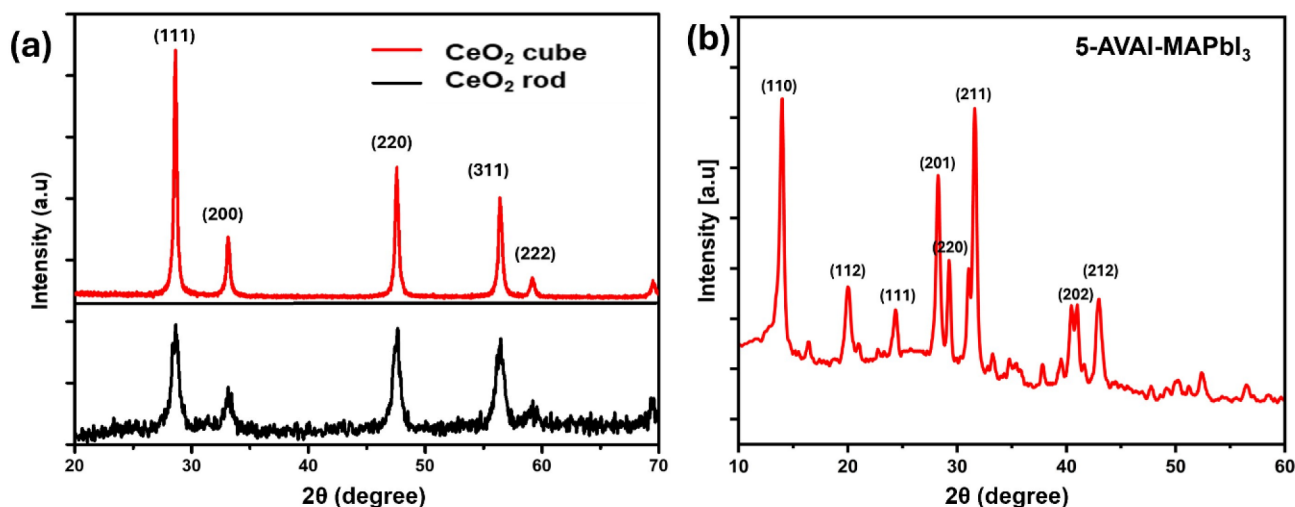


Figure 2. XRD patterns of the (a) CeO_2 nanostructures and (b) 5-AVAI-MAPbI₃, respectively.

adequate modifications were introduced in this work.⁴⁷ Three batches of C-PSCs with different configurations were fabricated for this study. The C-PSC configuration of each batch is given in Table 1. For the fabrication of all three batches, a 2 cm × 2 cm fluorine-doped tin oxide (FTO) glass substrate with a sheet resistance of 10 Ω sq⁻¹ was used. The FTO-coated glass substrate underwent an etching process with diluted HCl and Zn powder. Afterward, the standard cleaning procedures were performed for 20 min each in an ultrasonic bath using detergent, DI water, ethanol, and acetone. Next, an ozone–ultraviolet treatment was performed for 30 min. Subsequent to the standard cleaning procedure, for all three batches, a compact-TiO₂ (c-TiO₂) solution was prepared with titanium diisopropoxide bis(acetylacetonate) (TDBA) (75 wt % in isopropanol, Sigma-Aldrich) in 2-propanol (1:7 v/v) for deposition. Then, for the entire batches, the c-TiO₂ layer was spin-coated at 5000 rpm for 30 s and annealed for 30 min at 500 °C. After cooling down the substrates to room temperature, diluted TiO₂ paste purchased from the Great Cell Solar Company (18NRT, w/w = 1:3.5 in ethanol) was spin-coated on all three batches at 4000 rpm for 30 s, followed by an annealing process at 500 °C for 30 min and cooling down to room temperature. Then, for the second and third batches, the suspensions of the synthesized CeO₂ rods and cubes in cyclohexane were spin-coated at 2000 rpm for 30 s, respectively. To understand the effect of thickness, the CeO₂ layer was also spin-coated at 1000 and 3000 rpm for a separate batch of devices. Subsequently, these batches were annealed at 150 °C for 30 min and gradually cooled to room temperature.

Afterward, for all the batches, the Al₂O₃ mesoporous layer was spin-coated with the diluted Al₂O₃ paste (Sigma-Aldrich, 702129; v/v = 1:2 in isopropanol) at 3000 rpm for 30 s. Then, the substrates were annealed at 150 °C for 30 min and prepared for the carbon coating. The high-temperature carbon paste was prepared as per the previously published report with suitable modifications.⁴⁸ The carbon layer screen was printed for all the substrates and annealed at 450 °C for 1 h. After cooling down to room temperature, the prepared perovskite precursor solution was drop-casted over the coated carbon layer and spin-coated for 20 s at 1500 rpm. The perovskite solution was prepared by using the ion-exchange method following our previous report: 0.191 g of methylammonium iodide (MAI), 0.553 g of lead iodide (PbI₂), and 0.015 g of 5-

aminovaleric acid iodide (5-AVAI) were mixed in 1 mL of γ -butyrolactone (GBL). This was followed by heating at 70 °C for 30 min and a filtration technique using a 0.2- μm PTFE filter to remove the sediments from the prepared perovskite precursor solution.⁴⁷ At last, all of the batches underwent performance testing and characterization. The whole fabrication process and testing were performed under ambient conditions.

3. CHARACTERIZATION TECHNIQUES

The morphological analysis of the synthesized CeO₂ rod and cube particles was performed by scanning electron microscopy (SEM, LEO 430i, Carl Zeiss). The particle shape analysis was conducted at a magnification of 50 K \times , and the cross-sectional layer analysis at a magnification of 700 \times . The X-ray diffraction (XRD) of the material was executed by using X'pert pro-MPD XRD system from PANanalytical with Cu K α 1 radiation ($\lambda = 1.5406$ Å). The photovoltaic performance of the fabricated devices was evaluated with a Wacom AAA continuous solar simulator (model: WXS-210S-20, AM 1.5 G) under 1000 W/m² illumination and an I–V tracer (EKO MP-160i). The EIS (electrochemical impedance spectroscopy) was executed through an AUTOLAB frequency analyzer setup equipped with both an FRA (frequency response analyzer) module and an AUTOLAB PGSTAT 10. The EIS measurement was carried out under dark conditions with an open-circuit voltage of 0.80 V and a frequency range of 1 MHz to 0.1 Hz. In order to fit the experimental data, the Z-view software (Version 3.4d, Scribner Associates, Inc., USA) was used. The IPCE (incident photon-to-current efficiency) and EQE (external quantum efficiency) were measured by using the BENTHAM PVE300 instrument equipped with a tungsten halogen lamp source, which provided a wavelength range of 350–750 nm. In order to analyze the diffused reflectance, a spectrophotometer (PerkinElmer Lambda 1050) study was conducted for three types of samples.^{49–51} The first sample was prepared by coating c-TiO₂ and m-TiO₂ on the FTO glass sheets, and the other two were prepared by coating a thin layer of the synthesized CeO₂ nanostructures.

4. RESULTS AND DISCUSSION

4.1. Chemical Composition and Structural Analysis.

In order to determine the nature of the synthesized material,

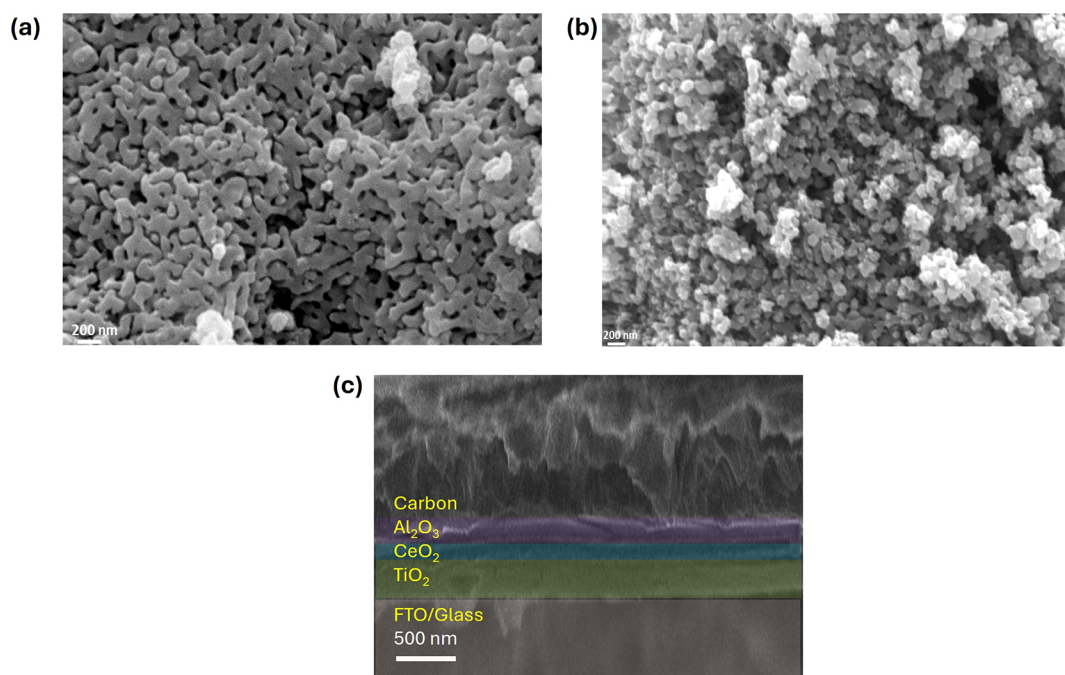


Figure 3. Microscopic characteristics of the materials: (a) SEM image for the CeO₂ rod particles, (b) SEM image for the synthesized CeO₂ cube particles, and (c) cross-sectional SEM image of a fabricated perovskite device showcasing different layers.

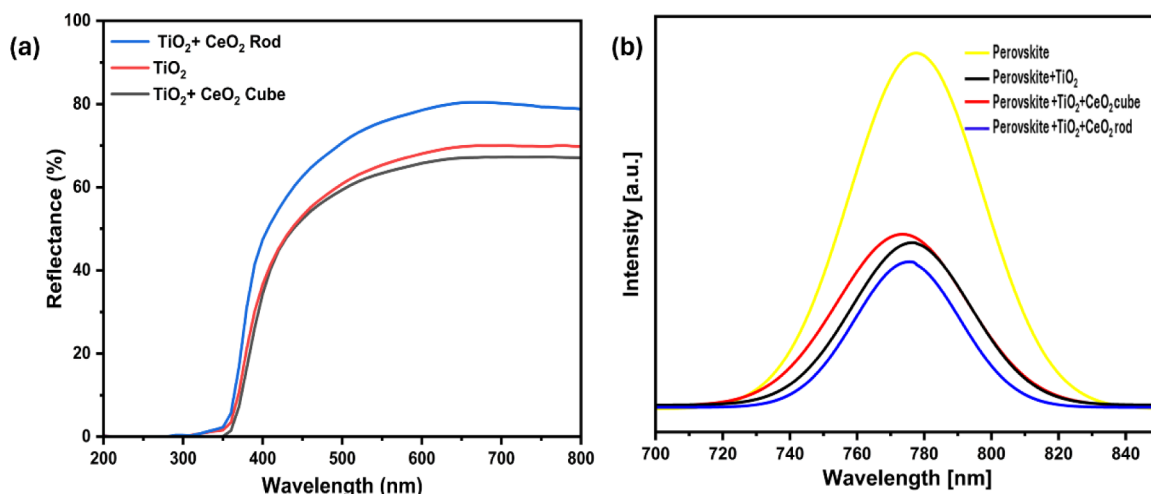


Figure 4. (a) Diffused reflectance analysis of the sample through the spectrophotometer study. (b) Steady-state photoluminescence pattern of the perovskite in the presence of the ETL.

both chemical composition and microstructural studies were carried out. XRD studies were conducted to pinpoint the composition and crystalline nature of the materials. Since different crystalline materials possess unique diffraction patterns, Figure 2a represents the XRD pattern for the synthesized CeO₂ nanostructures. The intensity of the diffraction peaks denotes the quantification of the relative amounts of the different phases in the synthesized sample. Figure 2a shows the XRD peaks near 28.80°, 33.50°, 47.60°, 56.70°, and 58.5° due to the (111), (200), (220), (311), (231), and (222) planes as the primary attributes of the sample. The peak planes resemble the crystalline phase of the CeO₂ particles.^{52–54} The sharper peaks of the nanocubes indicated their higher crystallinity and larger crystallite size compared to those of the nanorods. Nanorods showed anisotropic peak broadening due to their elongated shape,

while nanocubes exhibit more symmetric peak profiles. Similarly, the major peaks at ≈14°, 24.4°, 28.4°, and 31.8°, equivalent to the (110), (111), (201), and (211) planes, as displayed in Figure 2b, confirm the crystalline nature of the AVAI-MAPbI₃ perovskite.⁵⁵

The morphological variations of nanostructures usually have a critical effect on the reactivity, carrier mobility, and interface quality of thin-film devices.^{56,57} To understand the morphological difference of the synthesized nanostructures, SEM (scanning electron microscopy) was conducted. Figure 3a,b represents the rod and cubical structures, respectively, which resemble those observed in the previous study.⁴⁶ In comparison with the well-defined facets and edges of the cube structure, the rod structure is elongated in one direction. Through the analysis of the microscopic images, it was found that the average diameter of the synthesized nanorods is nearly

40 nm, whereas the average length of the rod particles is ~ 200 nm. On the other hand, the cube-like structure has an average crystallite size of ~ 50 nm.

Moreover, Figure 3c shows a cross-sectional view of a fully fabricated perovskite device. Scaling and analysis dictate the thicknesses of the layers as ~ 350 , ~ 160 , and ~ 240 nm for TiO_2 , CeO_2 , and Al_2O_3 , respectively, on FTO-coated glass. Furthermore, as perovskite is infiltrated on top of the carbon layer, it is not expected that perovskite plates will be observed in the cross-sectional SEM image.

4.2. Spectroscopic Analysis. As the diffused reflectance study provides a better understanding of the light scattering effect through the perovskite layer, the spectrophotometer study of the three different samples was conducted, namely glass/ TiO_2 , glass/ $\text{TiO}_2/\text{CeO}_2$ rod, and glass/ $\text{TiO}_2/\text{CeO}_2$ cube, as displayed in Figure 4a.⁵⁴ Considering the fact that the higher diffused reflectance is directly proportional to the light penetration toward the perovskite sensitizer, the sample consisting of TiO_2 and the CeO_2 rod structure provides the most favorable light diffusion, followed by TiO_2 and the combination of TiO_2 and the cube structure.^{54,58,59} Even though the thickness of TiO_2 remains unchanged for all of the samples, the changes in the diffused reflectance with respect to the two different CeO_2 nanostructures indicate the effect of morphology and densely packed particles of thin films. Thus, the nanorods' 1D structure enhances the light harvesting efficiency of the device, which, according to the literature, should decrease the electron transfer time from the perovskite to the photoanode, influencing an elongated recombination process.

To substantiate the findings, the photoluminescence of various ETLs and perovskite contacts was examined, which provided a fundamental understanding of charge transfer and interface quality, as shown in Figure 4b. At an excitation wavelength of 473 nm, a strong band-edge emission peak was observed in the samples, which was nearly at 775 nm. As expected, the most intense emission peak was observed for the perovskite film coated on top of the glass, whereas the quenching effect was exhibited by samples having additional transport layers. Due to the quenching effect, the films' excited electrons will return to the ground state by energy transfer to the ETLs, which act as the quenching layer influencing charge transfer efficiency. In Figure 4b, the nanorod-structured $\text{CeO}_2/\text{TiO}_2$ as the ETL showed the most promising quenching effect with the frailest emission peak near 775 nm, which implies significant electronic energy release by energy transfer. However, previous studies indicate that photoluminescence behavior alone does not promise the suitable photovoltaic performance of devices due to other photoelectrical factors of the C-PSC.

Importantly, a significant shift in wavelength was detected for the CeO_2 rod toward the blue region in the PL spectra, which authenticates the passivation of deep-level traps at grain boundaries, reducing the recombination centers and impacting higher charge transfer for the perovskite film.⁶⁰ Similarly, reduced surface defects due to the diminished grain boundaries of nanorods are expected to play a key role in enhancing the electrical properties of the devices.

4.3. Photovoltaic Performance Analysis. In order to conduct the photovoltaic performance analysis, three batches of cells with the configuration mentioned in Table 1 were prepared, and the performance study was conducted. Additionally, the EQE (external quantum efficiency) and EIS

(electrochemical impedance spectroscopy) were investigated to analyze photovoltaic behavior and the effect of morphology modulations on the performance. Table 2 represents the

Table 2. Photovoltaic Performance Characteristics of the C-PSC Fabricated with Three Configurations under 1 Sun AM 1.5G with a 0.25 cm² Active Area

| Device Type | V_{oc} (mV) | J_{sc} (mA/cm ²) | Fill Factor (FF) | PCE (%) |
|------------------------------------|---------------|--------------------------------|------------------|---------|
| $\text{TiO}_2 + \text{CeO}_2$ rod | 946.9 | 21.1 | 0.62 | 12.38 |
| $\text{TiO}_2 + \text{CeO}_2$ cube | 945.4 | 19.0 | 0.51 | 9.16 |
| TiO_2 only | 928.4 | 19.2 | 0.56 | 9.98 |

current density–voltage characteristics of different devices. In comparison to the results of the cells with the combined CeO_2 cube nanostructure and only TiO_2 ETLs, the cell configuration with the combined CeO_2 rod/ TiO_2 ETL showed the best performance. For the rod structure, the champion cell achieved a maximum PCE of 12.38% with a V_{oc} , J_{sc} , and FF of 946.96 mV, 21.1 mA/cm², and 0.620, respectively. Figure 5a exhibits the nature of the J – V curves of all three types of champion devices. From the high fill factor, it can be inferred that the TiO_2 modified with the CeO_2 nanorod reduces the loss of photoexcited carriers, suppressing surface electron recombination. Meanwhile, the increase in J_{sc} is mainly due to the high light-harvesting efficiency toward the photosensitizer. The results obtained from the photovoltaic performance study of all three batches align with the spectroscopic analysis findings.

To understand the effect of fabrication engineering, photovoltaic performance was observed for CeO_2 -based devices with varying spin-coating speeds, as detailed in Table 3. The observations suggested that 2000 rpm achieved the optimum thickness suitable for devices with nanorod and nanocube morphologies.

Next, the EQE (external quantum efficiency) analysis provides insight into the spectral performance of the C-PSC with three configurations across visible wavelengths of light.^{58,61,62} As shown in Figure 5b, the cell configuration with the CeO_2 rod structure demonstrates the highest EQE of $\sim 92\%$ compared to those of the other two configurations. This indicates that the rod surface morphology reduces light trapping and enhances scattering effects within the device.^{63–65} The integrated photocurrent density was calculated from the IPCE measurement (inset, Figure 5b) and found to be around 18.5 mA/cm², 16.7 mA/cm², and 16.5 mA/cm² for CeO_2 rod/ TiO_2 , only TiO_2 , and CeO_2 cube/ TiO_2 devices, respectively. The effect of optical losses caused by transmission and reflection produced slightly reduced values of integrated photocurrent densities compared to the values obtained via J – V characterization. Noticeably, strong IPCE coverage in the range of ~ 500 to 780 nm for CeO_2 rod-based devices demonstrates significant improvement in interface quality and proficient charge carrier transport compared to the commercial TiO_2 -based ETL, certifying the surface defect reduction.³⁸

The EIS analysis implicates the rationale behind the changes in the C-PSC performance metrics such as V_{oc} , J_{sc} , and FF of each cell. The representation of EIS reveals information about the transport process and charge carrier recombination of the perovskite layers at the interfaces or the adjacent layers.^{66–68} Primarily, this provides insight into the charge extraction process from the perovskite to the ETL and the perovskite to counter electrode interfaces.^{67–69} Figure 5c indicates the

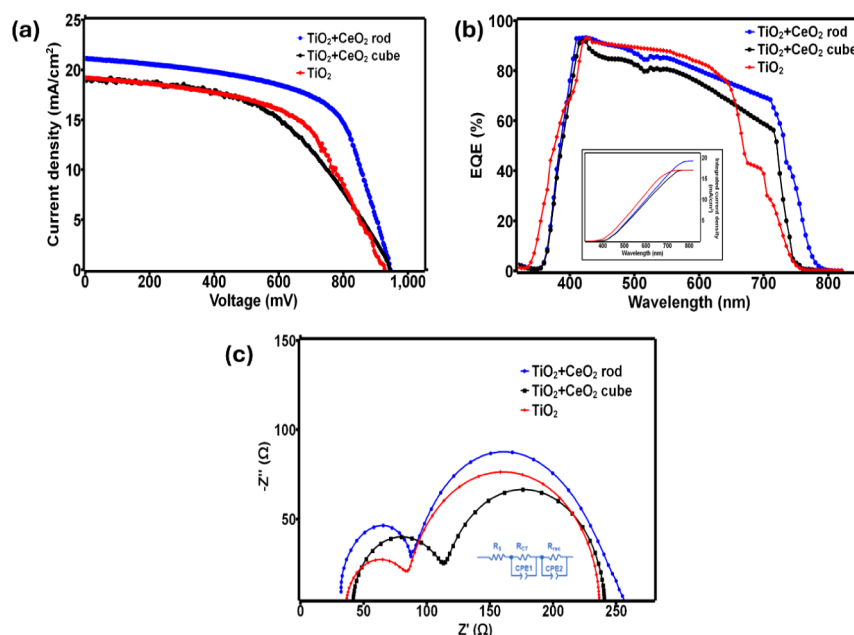


Figure 5. (a) Photovoltaic performance of the three devices with different configurations, (b) corresponding EQE representation of the devices (inset: integrated photocurrent density plot), and (c) EIS nature of the devices with the fitted electrical circuit diagram (inset: circuit diagram).

Table 3. Photovoltaic Performance of the Champion CeO₂ Nanostructure Devices at Different Spin-Coating Speeds under 1 Sun AM 1.5, Having an Active Area of 0.25 cm²

| Device | J_{sc} (mA/cm ²) | V_{oc} (mV) | Fill Factor (FF) | PCE (%) |
|--------------------------------|--------------------------------|---------------|------------------|---------|
| CeO ₂ rod 1000 rpm | 20.4 | 925.2 | 0.61 | 11.5 |
| CeO ₂ rod 3000 rpm | 20.8 | 932.6 | 0.615 | 11.9 |
| CeO ₂ cube 1000 rpm | 18.6 | 924.8 | 0.503 | 8.65 |
| CeO ₂ cube 3000 rpm | 18.9 | 934.4 | 0.506 | 8.9 |

impedance response of three C-PSCs with different combinations. The R_s (series resistance) indicates the impedance response of the cell between the two electrodes, which are FTO and carbon, and displays that the C-PSC configuration with a rod structure provides a lower R_s compared to the cube and the normal titania.^{54,66,70–73} The R_{CT} represents the resistance between the carbon and perovskite layers. The R_{rec} (charge recombination resistance) in the equivalent circuit diagram quantifies the resistance between the perovskite and ETLs.^{54,66–68,70–72} Commonly, a lower R_{CT} value favors the enhanced photocurrent density of the C-PSC due to the superior charge collection ability between the perovskite and the counter electrode.^{67,70,71} The differences in the R_{CT} values for the three configurations of C-PSCs are clearly visible in Figure 5c and Table 4.

Since the particle shape and size affect the photovoltaic performance of the C-PSCs, the grain boundary effect on the nanoparticle shape of CeO₂ with the cube structure hinders the enhancement of the photovoltaic performance of the cell.^{70,74}

Table 4. EIS Parameters of the Champion C-PSC Devices with and without CeO₂

| Device Type | R_s (Ω) | R_{CT} (Ω) | R_{rec} (Ω) |
|------------------------------------------|-----------|--------------|---------------|
| TiO ₂ + CeO ₂ rod | 32.1 | 57.1 | 182.2 |
| TiO ₂ + CeO ₂ cube | 42.6 | 75.2 | 130.3 |
| TiO ₂ only | 36.1 | 49.7 | 151.1 |

While the grain boundaries can act as recombination centers for the charge carriers, this increases the recombination rates and reduces the charge carrier lifetime.^{37,74–77} The lower R_{rec} value in the C-PSC with the cube structure mirrors the higher recombination process at the ETL and perovskite interface, which gradually reduces the photovoltaic performance of the cells.^{66,67,71} On the other hand, the higher R_{rec} value of the cell with the rod structure indicates a lower recombination rate, which gives an upper hand to the usage of rod-structured CeO₂ in the C-PSC. Overall, the lower R_{CT} and high R_{rec} values of the C-PSC with the CeO₂ rod make it a better candidate for the HTL-free carbon-based perovskite device compared to only commercial TiO₂ devices.

This highlights the need to detail the effects of nanostructures in perovskite photovoltaics, regarding enhanced light harvesting, electron transfer, and trap passivation. Nanorods offer distinct advantages over nanocubes in light harvesting and electron transfer in perovskite solar cells due to their unique one-dimensional structure, which results in a higher aspect ratio, allowing them to scatter and trap light more effectively compared to nanocubes. This increases the optical path length, leading to better light absorption by the perovskite layer.^{78,79} The one-dimensional structure of nanorods provides a direct pathway for electron transport, reducing recombination losses. This anisotropic charge transport is more efficient than the random pathways in cube-based systems, leading to faster and more reliable electron transfer from the perovskite to the photoanode.⁷⁸ Further, nanorods minimize electron trapping sites and recombination rates due to their well-aligned structure, which is less prone to defects compared to the aggregated nature of nanoparticles.⁷⁹ Moreover, nanorods create a more uniform and intimate contact with the perovskite layer, enhancing charge injection and overall device performance.⁸⁰ Consequently, rod-type nanostructures have distinct advantages in passivating perovskite traps compared to nanocubes, largely due to their elongated shape, anisotropic properties, and unique interactions with perovskite materials. The rods can integrate more

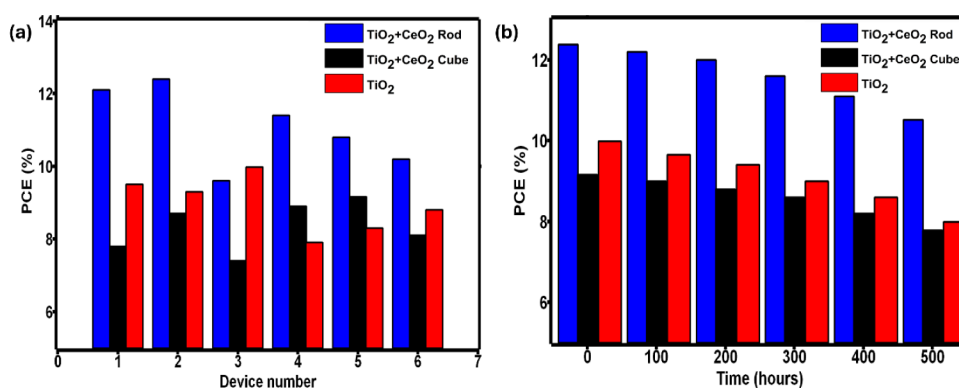


Figure 6. (a) Repeatability test for a batch of 6 devices from each type and (b) stability data (PCE vs time) of different types of devices after 500 h while maintained under ambient conditions.

effectively within the perovskite matrix due to their anisotropic structure. Their directional orientation supports better alignment with perovskite grains, optimizing the suppression of defect states.⁸¹ Unlike nanocubes, rod-type nanostructures facilitate directional charge transport through their elongated geometry. This reduces charge carrier losses and enhances overall device efficiency.⁸² Furthermore, the elongated shape allows rods to interact with defects that might be less accessible to smaller nanocubes. This leads to more thorough trap passivation and stabilization.⁸³

Similarly, grain boundaries in nanorods and nanocubes have distinct effects on the electron transport layer (ETL) in perovskite solar cells due to their differing morphologies and structural characteristics. Grain boundaries in nanorods are aligned along their elongated structure, which facilitates the directional charge transport. This reduces recombination losses and enhances the efficacy of the ETL.⁸⁴ Also, 1D nanorods can penetrate deeper into the perovskite layer, addressing defects at grain boundaries more effectively. This leads to improved trap passivation and stability. On the other hand, grain boundaries in nanocubes are distributed isotropically, which can lead to uniform but less directional charge transport. This may result in higher recombination losses compared to nanorods.⁸⁵ Ultimately, the reason for photovoltaic performance variation due to the morphology alteration is clear from the diffuse reflectance, PL, EQE, and EIS characterization.

Finally, the repeatability test was performed (Figure 6a), and the stability of the devices was observed under ambient conditions, monitored for 500 h, with photovoltaic characterization performed every 100 h (Figure 6b). The repeatability test for a batch of 6 devices produced average efficiencies of 11.0%, 8.3%, and 8.9% for the CeO₂ rod, CeO₂ cube, and pristine TiO₂-type devices, respectively. On the other hand, only 15% efficiency loss was observed for the CeO₂ devices during stability testing, whereas ~20% PCE loss was observed for TiO₂ devices. Some studies have described the extraction of electrons from I⁻ by TiO₂ and oxidizing I⁻ to iodine in the presence of light as a deforming factor of the perovskite crystal structure; as a result, slightly low stability was observed for commercial TiO₂-based devices.^{86,87} However, the presence of CeO₂ neutralizes this effect to a great extent, demonstrating a noteworthy stability improvement in the respective devices. The aim of this work is to discuss the morphological effect of nanomaterials and device engineering combinations, and we believe this study can provide further advancements in the field of perovskite photovoltaics.

5. CONCLUSION

In conclusion, two different CeO₂ nanostructures, rod and cube, were synthesized and added over the TiO₂ layer of the C-PSC. Integrally, the combination of TiO₂ and morphology-modulated CeO₂ acts as the ETL for the C-PSC, and the major part of the analysis was carried out by comparing the combined ETL and the normal ETL effects on the C-PSC. The device engineering showcased due to the CeO₂ nanostructures transformed the electron transfer property, light-harvesting efficiency, and the photovoltaic performance of the C-PSCs significantly. The cell configuration with the rod nanostructure indicated the highest PCE performance of 12.38% over 9.16% and 9.98% of the cube structure and the normal TiO₂, respectively. This suggests that the morphology modulation of the nanoparticles and allied grain boundary trap passivation contributes significantly to the performance of the C-PSCs. Moreover, the spectrophotometer and EIS analysis provided a better understanding of the effect of charge recombination rates on morphology modulation. The variations in the diffused reflectance denote the correlation effect of the light-scattering effect of the morphology-modulated CeO₂ and the combined effect with the TiO₂ particles toward better light harvesting. The results from the experimentation establish a foundation for the significant importance of morphology-modulated nanostructures and fabrication engineering of the devices in the field of HTL-free C-PSCs. From this work, we anticipate that the results may open up pathways for future advancements in the morphology optimization of nanomaterials for C-PSC application and facilitate their feasible integration into real-world applications.

■ ASSOCIATED CONTENT

Data Availability Statement

The dataset is available on request.

■ AUTHOR INFORMATION

Corresponding Authors

Shubhranshu Bhandari – Solar Energy Research Group, Environment and Sustainability Institute, University of Exeter, Cornwall TR10 9FE, U.K.; orcid.org/0000-0002-3347-9682; Email: s.bhandari@exeter.ac.uk

Sreeram Valsalakumar – Solar Energy Research Group, Environment and Sustainability Institute, University of Exeter, Cornwall TR10 9FE, U.K.; Email: sv353@exeter.ac.uk

Authors

Mir Sahidul Ali – Department of Polymer Science and Technology, University of Calcutta, Kolkata, West Bengal 700009, India; orcid.org/0000-0002-7082-7447

Tapas K. Mallick – Solar Energy Research Group, Environment and Sustainability Institute, University of Exeter, Cornwall TR10 9FE, U.K.

Justin Hinshelwood – Faculty of Environment Science and Economy, University of Exeter, Cornwall TR10 9FE, U.K.

Senthilarasu Sundaram – School of Computing, Engineering and Design Technologies, Teesside University, Middlesbrough TS1 3BX, U.K.

Complete contact information is available at:
<https://pubs.acs.org/10.1021/acs.energyfuels.5c00518>

Author Contributions

#S.B. and S.V. have the same contribution as the lead authors. S.B. and S.V.: conceptualization, investigation, methodology, data curation, analysis, writing – original draft, writing – review and editing, and visualization. M.S.A.: investigation, methodology, analysis, writing – review and editing, and visualization. T.K.M., J.H., and S.S.: writing – review and editing, supervision, project administration, and funding acquisition.

Funding

This research was funded by the Engineering and Physical Sciences Research Council, UK: PhD Fellowship, and the Engineering and Physical Sciences Research Council, UK: EP/T025875/1. The work is also supported by funding from an EPSRC-funded project called “Advanced Building Façade Design for Optimal Delivery of End Use Energy Demand” (EP/S030786/1).

Notes

The authors declare no competing financial interest.

ACKNOWLEDGMENTS

SV acknowledges the Engineering and Physical Sciences Research Council for the PhD fellowship. MSA is thankful to the Council of Scientific & Industrial Research (CSIR), Government of India, for the Senior Research Fellowship (SRF-Direct) (File no: 09/0028(18530)/2024-EMR-I). For the purpose of open access, the author has applied a 'Creative Commons Attribution (CC BY)' licence to any Author Accepted Manuscript version arising from this submission.

REFERENCES

- (1) Green, M. A.; Ho-Baillie, A.; Snath, H. J. The Emergence of Perovskite Solar Cells. *Nat. Photonics* **2014**, *8* (8), 506–514.
- (2) Kim, J. Y.; Lee, J.-W.; Jung, H. S.; Shin, H.; Park, N.-G. High-Efficiency Perovskite Solar Cells. *Chem. Rev.* **2020**, *120* (15), 7867–7918.
- (3) Li, D.; Zhang, D.; Lim, K.-S.; Hu, Y.; Rong, Y.; Mei, A.; Park, N.-G.; Han, H. A Review on Scaling Up Perovskite Solar Cells. *Adv. Funct. Mater.* **2021**, *31* (12), 2008621.
- (4) Wu, T.; et al. The Main Progress of Perovskite Solar Cells in 2020–2021: Tin-Based Perovskite Solar Cells, Additive Engineering, Heterostructure Stabilization, Cell Encapsulation, Si/Perovskite Tandem, All-Perovskite Tandem, Back Electrode. *Nano-Micro Lett.* **2021**, *13*, 152.
- (5) Taylor, A. D.; et al. A General Approach to High-Efficiency Perovskite Solar Cells by Any Antisolvent. *Nat. Commun.* **2021**, *12* (1), 1878.

(6) Yoo, J. J.; et al. Efficient Perovskite Solar Cells via Improved Carrier Management. *Nature* **2021**, *590* (7847), 587–593.

(7) Jeong, M.; et al. Stable Perovskite Solar Cells with Efficiency Exceeding 24.8% and 0.3-V Voltage Loss. *Science* **2020**, *369* (6511), 1615–1620.

(8) Nair, S.; Patel, S. B.; Gohel, J. V. Recent Trends in Efficiency-Stability Improvement in Perovskite Solar Cells. *Mater. Today Energy* **2020**, *17*, 100449.

(9) Park, N.-G. Research Direction toward Scalable, Stable, and High-Efficiency Perovskite Solar Cells. *Adv. Energy Mater.* **2020**, *10* (13), 1903106.

(10) NREL Photovoltaic Research. *Interactive Best Research-Cell Efficiency Chart*. <https://www.nrel.gov/pv/interactive-cell-efficiency.html>. (Accessed 11 April 2025).

(11) Huang, Y.; et al. Towards Simplifying the Device Structure of High-Performance Perovskite Solar Cells. *Adv. Funct. Mater.* **2020**, *30* (28), 2000863.

(12) Faizan, M.; Bhamu, K. C.; Murtaza, G.; He, X.; Kulhari, N.; AL-Anazy, M. M.; Khan, S. H. Electronic and Optical Properties of Vacancy-Ordered Double Perovskites A_2BX_6 (A = Rb, Cs; B = Sn, Pd, Pt; and X = Cl, Br, I): A First-Principles Study. *Sci. Rep.* **2021**, *11* (1), 6965.

(13) Sa, R.; Wei, Y.; Zha, W.; Liu, D. A first-principle study of the structural, mechanical, electronic and optical properties of vacancy-ordered double perovskite Cs_2TeX_6 (X = Cl, Br, I). *Chem. Phys. Lett.* **2020**, *754*, 137538.

(14) Bendib, T.; et al. Combined Optical-Electrical Modeling of Perovskite Solar Cell with an Optimized Design. *Opt. Mater.* **2020**, *109*, 110259.

(15) Hossain, M. K.; Rubel, M. H. K.; Toki, G. F. I.; Alam, I.; Rahman, M. F.; Bencherif, H. Effect of Various Electron and Hole Transport Layers on the Performance of $CsPbI_3$ -Based Perovskite Solar Cells: A Numerical Investigation in DFT, SCAPS-1D, and wxAMPS Frameworks. *ACS Omega* **2022**, *7* (47), 43210–43230.

(16) Aitola, K.; Sonai, G. G.; Markkanen, M.; Kaschuk, J. J.; Hou, X.; Miettunen, K.; Lund, P. D. Encapsulation of Commercial and Emerging Solar Cells with Focus on Perovskite Solar Cells. *Sol. Energy* **2022**, *237*, 264–283.

(17) Li, H.; Cui, C.; Xu, X.; Bian, S.; Ngaojampa, C.; Ruankham, P.; Jaroenjittchai, A. P. A Review of Characterization of Perovskite Film in Solar Cells by Spectroscopic Ellipsometry. *Sol. Energy* **2020**, *212*, 48–61.

(18) Hossain, M. I.; et al. Electrical and Optical Properties of Nickel-Oxide Films for Efficient Perovskite Solar Cells. *Small Methods* **2020**, *4* (9), 2000454.

(19) Ahläng, C.; Nyman, M.; Österbacka, R. Influence of the Electric Potential on Charge Extraction and Interface Recombination in Perovskite Solar Cells. *Phys. Rev. Appl.* **2021**, *16*, 014041.

(20) Shi, X.; Chen, R.; Jiang, T.; Ma, S.; Liu, X.; Ding, Y.; Cai, M.; Wu, J.; Dai, S. Regulation of Interfacial Charge Transfer and Recombination for Efficient Planar Perovskite Solar Cells. *Sol. RRL* **2020**, *4* (2), 1900198.

(21) Odunmbaku, G. O.; et al. Recombination Pathways in Perovskite Solar Cells. *Adv. Mater. Interfaces* **2022**, *9* (24), 2102137.

(22) Mozaffari, N.; et al. Unraveling the Role of Energy Band Alignment and Mobile Ions on Interfacial Recombination in Perovskite Solar Cells. *Sol. RRL* **2022**, *6* (3), 2101087.

(23) Wu, W.-Q.; Liao, J.-F.; Zhong, J.-X.; Xu, Y.-F.; Wang, L.; Huang, J. Suppressing Interfacial Charge Recombination in Electron-Transport-Layer-Free Perovskite Solar Cells to Give an Efficiency Exceeding 21%. *Angew. Chem., Int. Ed.* **2020**, *59* (47), 20980–20987.

(24) Prochowicz, D.; Tavakoli, M. M.; Wolska-Pietkiewicz, M.; Jędrzejewska, M.; Trivedi, S.; Kumar, M.; Zakeeruddin, S. M.; Lewiński, J.; Graetzel, M.; Yadav, P. Suppressing Recombination in Perovskite Solar Cells via Surface Engineering of TiO_2 ETL. *Sol. Energy* **2020**, *197*, 50–57.

(25) Jeyakumar, R.; Bag, A.; Nekovei, R.; Radhakrishnan, R. Influence of Electron Transport Layer (TiO_2) Thickness and Its

- Doping Density on the Performance of $\text{CH}_3\text{NH}_3\text{PbI}_3$ -Based Planar Perovskite Solar Cells. *J. Electron. Mater.* **2020**, *49* (6), 3533–3539.
- (26) Keshtrand, R.; Zamani-Meymian, M. R.; Taghavinia, N. Improving the Performance of Planar Perovskite Solar Cell Using NH_4Cl Treatment of SnO_2 as Electron Transport Layer. *Surf. Interfaces* **2022**, *28*, 101596.
- (27) Haque, M. M.; Mahjabin, S.; Rashid, M. J.; Alharbi, H. F.; Suemasu, T.; Akhtaruzzaman, M. Exploring the Effect of Interface Properties Between CeOx Electron Transport Layer and MAPbI₃ Perovskite Layer on Solar Cell Performances Through Numerical Simulation. *Jpn. J. Appl. Phys.* **2023**, *63*, 012001.
- (28) Ahmmed, S.; Aktar, A.; Rahman, M. H.; Hossain, J.; Ismail, A. B. M. Design and Simulation of a High-Performance $\text{CH}_3\text{NH}_3\text{Pb}(\text{I}-\text{xCl})_3$ -Based Perovskite Solar Cell Using a CeOx Electron Transport Layer and NiO Hole Transport Layer. *Semicond. Sci. Technol.* **2021**, *36* (2), 035002.
- (29) Song, J.; Yang, Y.; Zhao, Y. L.; Che, M.; Zhu, L.; Gu, X. Q.; Qiang, Y. H. Morphology Modification of Perovskite Film by a Simple Post-Treatment Process in Perovskite Solar Cell. *Mater. Sci. Eng., B* **2017**, *217*, 18–25.
- (30) Tailor, N. K.; Abdi-Jalebi, M.; Gupta, V.; Hu, H.; Dar, M. I.; Li, G.; Satapathi, S. Recent Progress in Morphology Optimization in Perovskite Solar Cell. *J. Mater. Chem. A* **2020**, *8* (41), 21356–21386.
- (31) Wang, M.; Yin, Y.; Cai, W.; Liu, J.; Han, Y.; Feng, Y.; Dong, Q.; Wang, Y.; Bian, J.; Shi, Y. Synergetic Co-Modulation of Crystallization and Co-Passivation of Defects for FAPbI₃ Perovskite Solar Cells. *Adv. Funct. Mater.* **2022**, *32* (6), 2108567.
- (32) Milić, J. V.; Kubicki, D. J.; Emsley, L.; Grätzel, M. Multifunctional Molecular Modulation for Efficient and Stable Hybrid Perovskite Solar Cells. *Chimia* **2019**, *73* (5), 317–322.
- (33) Wu, X.; et al. All-Inorganic CsPbI₂Br Perovskite Solar Cell with Open-Circuit Voltage Over 1.3 V by Balancing Electron and Hole Transport. *Sol. RRL* **2022**, *6* (8), 2200171.
- (34) Wang, H.; et al. Ligand-Modulated Excess PbI₂ Nanosheets for Highly Efficient and Stable Perovskite Solar Cells. *Adv. Mater.* **2020**, *32* (32), 2000865.
- (35) Wu, M.-C.; et al. Achieving High-Performance Perovskite Photovoltaic by Morphology Engineering of Low-Temperature Processed Zn-Doped TiO₂ Electron Transport Layer. *Small* **2020**, *16* (38), 2002201.
- (36) Khan, J.; Rahman, N. U.; Khan, W. U.; Wang, Y.; Fu, S.; Ahmed, G.; Akhtar, M. N.; Wu, M. Hollow 3D TiO₂ Sub-Microspheres as an Electron Transporting Layer for Highly Efficient Perovskite Solar Cells. *Mater. Today Energy* **2021**, *19*, 100614.
- (37) Wang, F.; Yang, M.; Zhang, Y.; Du, J.; Han, D.; Yang, L.; Fan, L.; Sui, Y.; Sun, Y.; Meng, X.; et al. Constructing m-TiO₂/a-WOx hybrid electron transport layer to boost interfacial charge transfer for efficient perovskite solar cells. *Chem. Eng. J.* **2020**, *402*, 126303.
- (38) Bhandari, S.; Roy, A.; Mallick, T. K.; Sundaram, S. Morphology Modulated Brookite TiO₂ and BaSnO₃ as Alternative Electron Transport Materials for Enhanced Performance of Carbon Perovskite Solar Cells. *Chem. Eng. J.* **2022**, *446*, 137378.
- (39) Arshad, Z.; et al. Performance Analysis of Calcium-Doped Titania (TiO₂) as an Effective Electron Transport Layer (ETL) for Perovskite Solar Cells. *Energies* **2022**, *15* (4), 1408.
- (40) Ebrahimi, M.; Kermandpur, A.; Atapour, M.; Adhami, S.; Heidari, R. H.; Khorshidi, E.; Irannejad, N.; Rezaie, B. Performance Enhancement of Mesoscopic Perovskite Solar Cells with GQDs-Doped TiO₂ Electron Transport Layer. *Sol. Energy Mater. Sol. Cells* **2020**, *208*, 110407.
- (41) Luo, J.; Zhu, J.; Lin, F.; Xia, J.; Yang, H.; Yang, J.; Wang, R.; Yuan, J.; Wan, Z.; Li, N.; et al. Molecular Doping of a Hole-Transporting Material for Efficient and Stable Perovskite Solar Cells. *Chem. Mater.* **2022**, *34* (4), 1499–1508.
- (42) Kim, M.; Choi, I.-W.; Choi, S. J.; Song, J. W.; Mo, S.-I.; An, J.-H.; Jo, Y.; Ahn, S.; Ahn, S. K.; Kim, G.-H.; et al. Enhanced Electrical Properties of Li-Salts Doped Mesoporous TiO₂ in Perovskite Solar Cells. *Joule* **2021**, *5* (3), 659–672.
- (43) Liu, D.; Li, S.; Zhang, P.; Wang, Y.; Zhang, R.; Sarvari, H.; Wang, F.; Wu, J.; Wang, Z.; Chen, Z. D. Efficient Planar Heterojunction Perovskite Solar Cells with Li-Doped Compact TiO₂ Layer. *Nano Energy* **2017**, *31*, 462–468.
- (44) Teimouri, R.; Heydari, Z.; Ghaziani, M. P.; Madani, M.; Abdy, H.; Kolahdouz, M.; Asl-Soleimani, E. Synthesizing Li-Doped TiO₂ Electron Transport Layers for Highly Efficient Planar Perovskite Solar Cell. *Superlattices Microstruct.* **2020**, *145*, 106627.
- (45) Giordano, F.; et al. Enhanced Electronic Properties in Mesoporous TiO₂ via Lithium Doping for High-Efficiency Perovskite Solar Cells. *Nat. Commun.* **2016**, *7*, 10379.
- (46) Kovacevic, M.; Mojet, B. L.; Van Ommen, J. G.; Lefferts, L. Effects of Morphology of Cerium Oxide Catalysts for Reverse Water Gas Shift Reaction. *Catal. Lett.* **2016**, *146* (4), 770–777.
- (47) Valsalakumar, S.; Bhandari, S.; Mallick, T. K.; Hinshelwood, J.; Sundaram, S. Experimental Validation of Optimized Solar Cell Capacitance Simulation for Rheology-Modulated Carbon-Based Hole Transport Layer-Free Perovskite Solar Cell. *Adv. Energy Sustain. Res.* **2024**, *5* (3), 300244.
- (48) Bhandari, S.; Mallick, T. K.; Sundaram, S. Enlightening the temperature coefficient of triple mesoscopic $\text{CH}_3\text{NH}_3\text{PbI}_{3-x}\text{Cl}_x/\text{NiO}$ and double mesoscopic CsFAMAPbI_{3-x}Br_x/CuSCN carbon perovskite solar cells. *J. Phys. Energy* **2023**, *5* (2), 025006.
- (49) Kim, D. I.; Lee, J. W.; Jeong, R. H.; Yang, J. W.; Park, S.; Boo, J.-H. Optical and Water-Repellent Characteristics of an Anti-Reflection Protection Layer for Perovskite Solar Cells Fabricated in Ambient Air. *Energy* **2020**, *210*, 118582.
- (50) Nguyen, H. T.; Gerritsen, S.; Mahmud, M. A.; Wu, Y.; Cai, Z.; Truong, T.; Tebyetekerwa, M.; Duong, T.; Peng, J.; Weber, K.; et al. Spatially and Spectrally Resolved Absorptivity: New Approach for Degradation Studies in Perovskite and Perovskite/Silicon Tandem Solar Cells. *Adv. Energy Mater.* **2020**, *10*, 1902901.
- (51) Rejaiba, O.; Khirouni, K.; Dhaou, M. H.; Alzahrani, B.; Bouazizi, M. L.; Khelifi, J. Investigation study of optical and dielectric parameters using absorption and diffuse reflectance spectroscopy method on La_{0.57}Nd_{0.13}Sr_{0.13}Ag_{0.2}MnO₃ perovskite for optoelectronic application. *Opt. Quantum Electron.* **2022**, *54* (5), 315.
- (52) Liu, B.; et al. Perovskite Solar Cells with Extremely High 24.63% Efficiency through Design of Double Electron Transport Layers and Double Luminescent Converter Layers. *Adv. Funct. Mater.* **2024**, *34* (10), 2401007.
- (53) Shi, C.; et al. Interface Modification via Rare Earth Material to Assist Hole Migration for Efficiency and Stability Promotion of Perovskite Solar Cells. *Sol. RRL* **2023**, *7* (5), 2300461.
- (54) Roy, A.; Bhandari, S.; Sundaram, S.; Mallick, T. K. Intriguing CeO₂-TiO₂ Hybrid Nanostructured Photoanode Resulting Up to 46% Efficiency Enhancement for Dye-Sensitized Solar Cells. *Mater. Chem. Phys.* **2021**, *272*, 125036.
- (55) Wei, N.; Chen, Y.; Miao, Y.; Zhang, T.; Wang, X.; Wei, H.; Zhao, Y. 5-Ammonium Valeric Acid Iodide to Stabilize MAPbI₃ via a Mixed-Cation Perovskite with Reduced Dimension. *J. Phys. Chem. Lett.* **2020**, *11* (19), 8170–8176.
- (56) Choi, H.; Choi, K.; Choi, Y.; Kim, T.; Lim, S.; Park, T. A Review on Reducing Grain Boundaries and Morphological Improvement of Perovskite Solar Cells from Methodology and Material-Based Perspectives. *Small Methods* **2020**, *4* (5), 1900569.
- (57) Kim, S. Y.; Cho, S. J.; Byeon, S. E.; He, X.; Yoon, H. J. Self-Assembled Monolayers as Interface Engineering Nanomaterials in Perovskite Solar Cells. *Adv. Energy Mater.* **2020**, *10* (40), 2002606.
- (58) Ma, C.; et al. Light Management in Highly-Textured Perovskite Solar Cells: From Full-Device Ellipsometry Characterization to Optical Modeling for Quantum Efficiency Optimization. *Sol. Energy Mater. Sol. Cells* **2021**, *230*, 111144.
- (59) Tooghi, A.; Fathi, D.; Eskandari, M. Numerical Study of a Highly Efficient Light Trapping Nanostructure of Perovskite Solar Cell on a Textured Silicon Substrate. *Sci. Rep.* **2020**, *10* (1), 18699.
- (60) Guo, Q.; et al. Low-Temperature Processed Rare-Earth Doped Brookite TiO₂ Scaffold for UV Stable, Hysteresis-Free, and High-Performance Perovskite Solar Cells. *Nano Energy* **2020**, *77*, 105183.

- (61) Chakraborty, J.; Islam, M. A.; Reza, S. Performance Analysis of Highly Efficient 2D/3D Bilayer Inverted Perovskite Solar Cells. *Sol. Energy* **2021**, *230*, 195–207.
- (62) Brinkmann, K. O.; et al. The Optical Origin of Near-Unity External Quantum Efficiencies in Perovskite Solar Cells. *Sol. RRL* **2021**, *5* (11), 2100371.
- (63) Bhattarai, S.; Hossain, I.; Maiti, M.; Pandey, R.; Madan, J. Performance Analysis and Optimization of All-Inorganic CsPbI₃-Based Perovskite Solar Cell. *Indian J. Phys.* **2023**, *97* (9), 2629–2637.
- (64) Cheng, Y.; et al. Revealing the Degradation and Self-Healing Mechanisms in Perovskite Solar Cells by Sub-Bandgap External Quantum Efficiency Spectroscopy. *Adv. Mater.* **2021**, *33* (2), 2006170.
- (65) Mercaldo, L. V.; et al. Procedure Based on External Quantum Efficiency for Reliable Characterization of Perovskite Solar Cells. *Energy Technol.* **2022**, *10* (9), 2200748.
- (66) Sadhukhan, P.; Ghosh, D.; Sengupta, P.; Bhattacharyya, S.; Das, S. Unraveling the Charge Transport Mechanism in Mechanochemically Processed Hybrid Perovskite Solar Cell. *Langmuir* **2021**, *37* (18), 5513–5521.
- (67) Ahmad, Z.; Mishra, A.; Abdulrahim, S. M.; Touati, F. Electrical Equivalent Circuit (EEC) Based Impedance Spectroscopy Analysis of HTM-Free Perovskite Solar Cells. *J. Electroanal. Chem.* **2020**, *871*, 114294.
- (68) Abdulrahim, S. M.; Ahmad, Z.; Bhadra, J.; Al-Thani, N. J. Long-Term Stability Analysis of 3D and 2D/3D Hybrid Perovskite Solar Cells Using Electrochemical Impedance Spectroscopy. *Molecules* **2020**, *25* (24), 5794.
- (69) Hailegnaw, B.; Sariciftci, N. S.; Scharber, M. C. Impedance Spectroscopy of Perovskite Solar Cells: Studying the Dynamics of Charge Carriers Before and After Continuous Operation. *Phys. Status Solidi A* **2020**, *217* (17), 2000291.
- (70) Chen, Y.; Wu, S.; Li, X.; Liu, M.; Chen, Z.; Zhang, P.; Li, S. Efficient and Stable Low-Cost Perovskite Solar Cells Enabled by Using Surface-Passivated Carbon as the Counter Electrode. *J. Mater. Chem. C* **2022**, *10* (3), 1270–1275.
- (71) Riquelme, A. J.; Valadez-Villalobos, K.; Boix, P. P.; Oskam, G.; Mora-Seró, I.; Anta, J. A.; et al. Understanding Equivalent Circuits in Perovskite Solar Cells: Insights from Drift-Diffusion Simulation. *Phys. Chem. Chem. Phys.* **2022**, *24* (26), 15657–15671.
- (72) Abdulrahim, S. M.; Ahmad, Z.; Bahadra, J.; Al-Thani, N. J. Electrochemical Impedance Spectroscopy Analysis of Hole Transporting Material-Free Mesoporous and Planar Perovskite Solar Cells. *Nanomaterials* **2020**, *10* (9), 1635.
- (73) Abdulrahim, S. M.; et al. Effect of Illumination and Applied Potential on the Electrochemical Impedance Spectra in Triple Cation (FA/MA/Cs) 3D and 2D/3D Perovskite Solar Cells. *J. Electroanal. Chem.* **2021**, *902*, 115800.
- (74) Gu, L.; Wang, S.; Chen, Y.; Xu, Y.; Li, R.; Liu, D.; Fang, X.; Jia, X.; Yuan, N.; Ding, J. Stable High-Performance Perovskite Solar Cells via Passivation of the Grain Boundary and Interface. *ACS Appl. Energy Mater.* **2021**, *4* (7), 6883–6891.
- (75) Jia, P.; et al. The Trapped Charges at Grain Boundaries in Perovskite Solar Cells. *Adv. Funct. Mater.* **2021**, *31* (14), 2107125.
- (76) Li, G.; Song, J.; Wu, J.; Song, Z.; Wang, X.; Sun, W.; Fan, L.; Lin, J.; Huang, M.; Lan, Z.; et al. Efficient and Stable 2D@3D/2D Perovskite Solar Cells Based on Dual Optimization of Grain Boundary and Interface. *ACS Energy Lett.* **2021**, *6* (10), 3614–3623.
- (77) Chen, R.; Feng, Y.; Zhang, C.; Wang, M.; Jing, L.; Ma, C.; Bian, J.; Shi, Y. Carbon-Based HTL-Free Modular Perovskite Solar Cells with Improved Contact at Perovskite/Carbon Interfaces. *J. Mater. Chem. C* **2020**, *8* (27), 9262–9270.
- (78) Srivastava, K. V.; Srivastava, P.; Srivastava, A.; Maurya, R. K.; Singh, Y. P.; Srivastava, A. 1D TiO₂ Photoanodes: A Game-Changer for High-Efficiency Dye-Sensitized Solar Cells. *RSC Adv.* **2025**, *15*, 4789–4819.
- (79) Wang, H.; Yan, L.; Liu, J.; Li, J.; Wang, H. Fabrication of Well-Aligned ZnO Nanorod Photoanodes for Perovskite Solar Cells. *J. Mater. Sci.: Mater. Electron.* **2016**, *27*, 6872–6880.
- (80) Ismail, M.; Olivier, C.; Toupance, T. Hybrid WO₃-Nanorods/TiO₂ Photoanodes for Improved Dye-Sensitized Solar Cell Performances under Back Illumination. *J. Mater. Sci.: Mater. Electron.* **2023**, *34*, 936.
- (81) Zhang, Z.; Qiao, L.; Meng, K.; Long, R.; Chen, G.; Gao, P. Rationalization of Passivation Strategies toward High-Performance Perovskite Solar Cells. *Chem. Soc. Rev.* **2023**, *52* (1), 163–195.
- (82) Qiu, X.; Liu, Y.; Li, W.; Hu, Y. Traps in Metal Halide Perovskites: Characterization and Passivation. *Nanoscale* **2020**, *12* (44), 22425–22451.
- (83) Wu, Y.; Wang, D.; Liu, J.; Cai, H. Review of Interface Passivation of Perovskite Layer. *Nanomaterials* **2021**, *11* (3), 775.
- (84) Noman, M.; Khan, Z.; Jan, S. T. A Comprehensive Review on the Advancements and Challenges in Perovskite Solar Cell Technology. *RSC Adv.* **2024**, *14*, 5085–5131.
- (85) Le, V. C.; Hoang, N. N.; Le, P. A.; et al. Synthesis and Characterization of TiO₂ Nanorods for Efficient Electronic Transport Layer of Perovskite Solar Cells. *J. Electron. Mater.* **2024**, *53*, 7291–7300.
- (86) Sugathan, V.; John, E.; Sudhakar, K. Recent Improvements in Dye-Sensitized Solar Cells: A Review. *Renewable Sustainable Energy Rev.* **2015**, *52*, 54–64.
- (87) Leijtens, T.; et al. Overcoming Ultraviolet Light Instability of Sensitized TiO₂ with Meso-Superstructured Organometal Tri-Halide Perovskite Solar Cells. *Nat. Commun.* **2013**, *4*, 2885.